ChemComm

COMMUNICATION

View Article Online
View Journal | View Issue



Cite this: *Chem. Commun.*, 2024, **60**, 9538

Received 30th June 2024,
Accepted 29th July 2024

DOI: 10.1039/d4cc03251a

rsc.li/chemcomm



# A smart roof that transforms raindrops into agricultural spraying†

Tao Shen,[ab] Can Gao,[bc] Xile Deng,*[d] Shijie Liu,[b] Zhuoxing Liu,[bc] Jia Peng,[bc] Jie Ma,[bc] Lianyang Bai,[d] Lei Jiang[ab] and Zhichao Dong*[bc]

**We present a smart roof that makes fragmented droplets from the impact of raindrops on superhydrophobic meshes and utilizes the droplets for agricultural spraying. This facile method transforms raindrops or waterdrops into uniform microdroplets, which can both reduce crop lodging induced by heavy rainfall, and realize uniform spraying of pesticides.**

Fragmentation is an atomization process and refers specifically to the division of a certain volume of drops into uniform microdroplets. Fragmentations of a liquid can be broadly classified as jet disintegration, sheet destabilization, filament breakage, raindrop deformation, *etc.*[1,2] Based on these principles, various approaches for achieving droplet fragmentation have been proposed including planar impact,[3,4] rotary centrifugation,[5] electrostatic manipulation,[6] and other atomizations using lasers,[7] ultrasonication[8] and electrospray.[9] Microdroplets with uniform diameters obtained using fragmentation can be applied in nanoparticle suspension printing,[10] medical research,[11] crop spraying,[12] *etc.*

Especially in agriculture, continuously and efficiently providing uniform microdroplets would address the challenges of nutrient replenishment during growth, pesticide loss during spraying, and soil sloughing during irrigation.[13–15] In general, crop leaves with relatively complex microstructures exhibit strong hydrophobicity.[16] As such, it is difficult for the pesticide or nutrient droplets to adhere to the hydrophobic or superhydrophobic leaves and perform their functions.[13] Even for hydrophilic leaves, facing intensive pesticide spraying or heavy rainfall impacts, crop lodging is inevitable. A millimeter-sized drop may generate collision forces thousands of times its own weight.[17] To avoid these problems, adjusting nozzle parameters, adding solvent additives and applying electrostatic field have all been utilized to acquire droplets of the appropriate size ($\approx$200 μm).[16,18] However, actualizing the aforementioned techniques, which have required delicate modifications or external energy inputs, is not simple.

A facile method involving droplets with a certain momentum impacting a superhydrophobic mesh realizes instantaneous fragmentation of the droplets.[12,19] In contrast to that for normal superhydrophobic surfaces,[20–22] the dynamics of spreading and penetration should be considered simultaneously for a droplet impacting a mesh with pores.[23] The size and rigidity of the mesh, and the velocity and size of the droplet are the main factors affecting the process of mesh impact-fragmentation.[24] In addition, the wettability, weaving form and features of the repeating unit of the mesh all contribute to the effect of fragmentation.[25–27] Nevertheless, from the perspective of practical applications, the evaluation system and application results of mesh impact-fragmentation are still lacking.

In the current work, we developed a rapid spraying method allowing for the fabrication of large-scale superhydrophobic metallic meshes. According to the fragmentation forms occurring at the mesh with various pore sizes, we defined the normalization factor $I^*$ to screen the optimal conditions for fragmentation. The penetration efficiency upon impact and the uniformity of microdroplets after fragmentation were also investigated. Finally, we demonstrated the feasibility of using the simple device for growing plants in the outdoors. Automatic transformation of raindrops and irrigated waterdrops into agricultural spraying with uniform microdroplets was also verified.

To prepare the superhydrophobic solution, 0.5 g of Capstone ST-200 (Dupont, USA), 1.0 g of hydrophobic fumed silica

[a] *Research Institute for Frontier Science, Key Laboratory of Bio-Inspired Smart Interfacial Science and Technology of Ministry of Education Beijing, School of Chemistry, Beihang University, Beijing 100191, People's Republic of China*
[b] *CAS Key Laboratory of Bio-inspired Materials and Interfacial Science, Technical Institute of Physics and Chemistry, Chinese Academy of Sciences, Beijing 100190, People's Republic of China. E-mail: dongzhichao@mail.ipc.ac.cn*
[c] *School of Future Technology & School of Nanoscience and Engineering, University of Chinese Academy of Sciences, Beijing 101407, People's Republic of China*
[d] *Key Laboratory for Biology and Control of Weeds, Hunan Academy of Agricultural Sciences, Changsha, Hunan 410125, People's Republic of China. E-mail: dengxile@hunaas.cn*

† Electronic supplementary information (ESI) available. See DOI: https://doi.org/10.1039/d4cc03251a

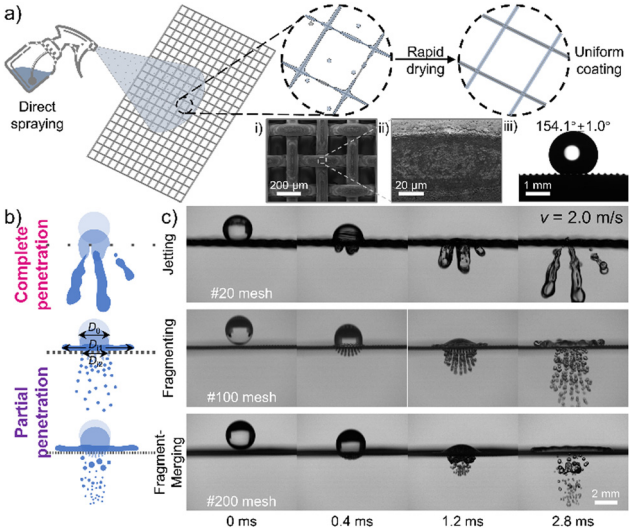


Fig. 1 Superhydrophobic mesh for smart roofs enable uniform spraying. (a) Schematic of the process of subjecting the superhydrophobic metallic mesh to a treatment of direct spraying and rapid drying. Insets show (i) and (ii) scanning electron microscopy (SEM) images and (iii) water contact angle of #100 superhydrophobic mesh after the treatment. (b) Sketches and (c) corresponding image sequences showing three modes of fragmentation after respective droplets impacted the superhydrophobic meshes with different mesh sizes.

nanoparticles (Evonik Degussa, Germany), and 50 ml of ethyl acetate (Innochem, China) were mixed, and then stirred in a sealed bottle for 1 h. Subsequently, a glass bottle was filled with the prepared superhydrophobic solution, which was sprayed directly onto the metallic mesh as shown in (Fig. 1a). Scanning electron microscopy (SEM) images showed that the rapid drying of the mesh that had been sprayed provided uniform coating of a single filament on the surface of the mesh (Fig. 1a, i and ii). The water contact angle of the treated #100 mesh was measured to be 154.1°± 1.0° (Fig. 1a, iii). Metallic meshes of different mesh sizes were also treated following the above method.

In order to investigate the effect of mesh size on the fragmentation, we used a high-speed camera (FASTCAM UX100) attached to a microscope lens (4×) to capture the droplet impact at 5000 frames per second (FPS). In the experiment, meshes of different mesh numbers were cut into 3 cm × 12 cm samples, which were then fixed to the apparatus printed by FDM printer (Pro2 Plus, Raise 3D, China) firmly to ensure no deformation (Fig. S2, ESI†). At the same Weber number ($We = \rho v^2 D_0/\gamma$, with $\rho$ denoting the liquid density, $v$ the speed of impact, $D_0$ the initial diameter of the droplet, and $\gamma$ the surface tension), different penetration modes after impact were identified, and are presented in (Fig. 1b).

At a lower mesh number, such as #20 mesh, the droplet was observed to pass directly through the superhydrophobic mesh by jetting, showing a mode involving complete penetration (Fig. 1c). With higher mesh number, the droplets shifted to a partial penetration mode, due to the decrease in the percentage of free space of the mesh. Upon impacting the superhydrophobic mesh, the droplets first divided into multiple ligaments, and then broke up into microdroplets, due to Plateau–Rayleigh instability.[1] Higher mesh numbers, meaning smaller mesh sizes, decreased the ligament width, resulting in microdroplets with smaller diameters after disturbance. Note that the microdroplet diameter did not decrease consistently with increasing mesh number. Comparing #100 and #200 meshes, we noticed smaller diameters of the microdroplets initially fragmented by the #200 mesh than those for the #100 mesh. But apparently the offset due to destabilization led to the merging of adjacent ligaments, in turn leading to an increase in the diameter and nonuniformity of the subsequently fragmented microdroplets (Fig. 1c).

To investigate the relationship between mesh size and droplet diameter, we selected seven superhydrophobic meshes with different mesh numbers. We came up with $I_i$ for evaluating the number of coverable mesh units before the droplet impacts the mesh (with $I_i$ calculated using the formula $I_i = D_0/(a_i + b_i)$, and $D_0$ denoting the initial diameter of the droplet, $a_i$ and $b_i$ denoting the width of a single wire and the free area, respectively, and subscript $i$ referring to the different mesh number). To normalize the variation of the mesh size and avoid other factors, we defined $I^*$ ($I^* = I_i/I_{\#20}$) as the scaling factor representing the mesh density (Fig. S1, ESI†). Here, #20 mesh—as the sparsest mesh of the samples tested—was chosen as the reference for further analysis. For the dynamics of the spreading and penetration of a droplet, we used $D_{i1}/D_0$ and $D_{i2}/D_0$ as maximum spreading and penetration factors. And the ratio of the penetration factor to the spreading factor was defined as the penetration efficiency ($D_{i2}/D_{i1}$), with $D_{i1}$ and $D_{i2}$ being the maximum diameters of spreading and penetration, respectively.

Our analyses indicated the spreading factor decreasing slightly with increasing $We$ number for low values of $I^*$, due to the larger mesh size through which the droplets can easily pass, but increasing with $We$ number for high values of $I^*$. However, the analyses also indicated a different relationship between the spreading factor and $We$ number for a droplet fragmented by a superhydrophobic mesh than the $D_{i1}/D_0 \sim We^{1/4}$ relationship observed for planar impacts (Fig. 2a).

After impacting a superhydrophobic mesh, whether droplet fragmentation occurs would be expected to depend on its inertial force. Our analyses indicated, as shown in (Fig. 2b), a higher $I^*$ being associated with a higher $We$ number, required to satisfy droplet fragmentation, with the critical $We$ number being linearly proportional to $I^*$. With an aim of screening the most suitable mesh for spraying, we focused on droplets with an impact velocity of 2.0 m $s^{-1}$ to analyse their spreading and penetration dynamics (Fig. 2c). With increasing $I^*$, the maximum spreading factor $D_{i1}/D_0$ was found to gradually increase and approach a constant value in the ideal superhydrophobic plane. Meanwhile, the maximum penetration factor $D_{i2}/D_0$ was found to show a trend of first increasing and then decreasing with increasing $I^*$. For a droplet impacting a single superhydrophobic filament, obstruction of the filament causes the droplet to elongate in the longitudinal direction. With an increasing number of impacting filaments, droplets were observed to preferentially spread above the mesh due to the difficulty of mass transferring limited by the filament blockage,

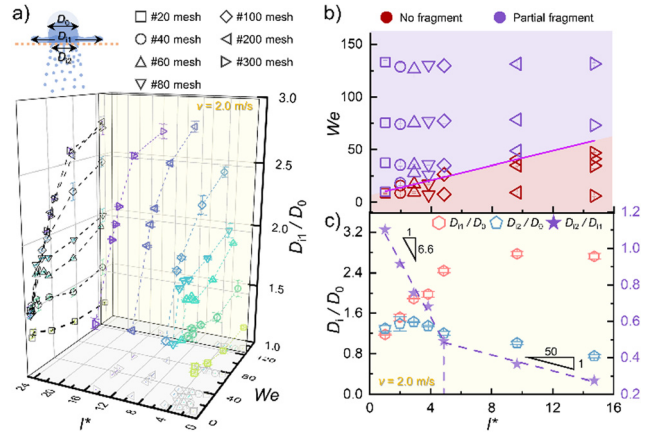


Fig. 2 Mesh parameters affect the effectiveness of spraying after impact. (a) Plot of the maximum spreading factor ($D_{i1}/D_0$) *versus* Weber number (*We*) and mesh density scaling factor (*I**), with *I** defined as the scaling factor representing the mesh density. (b) Phase diagram illustrating the fragmentation of a droplet impacting a superhydrophobic mesh for various *I** values. The purple line represents the boundary between no fragmentation and partial fragmentation regimes. (c) When the impact velocity of droplet is 2.0 m $s^{-1}$, the maximum spreading factor ($D_{i1}/D_0$) and penetration factor ($D_{i2}/D_0$) *versus* *I** are shown in the left axis, and the penetration efficiency ($D_{i2}/D_{i1}$) *versus* *I** are shown in the right axis. The two purple dashed lines are linear fittings of $D_{i2}/D_{i1}$ values to *I**, with values ranging from 1.00 to 4.85 and from 4.85 to 14.73, respectively. Data are shown each as mean ± SD ($n$ = 3, independent experiments), and the error bar represents SD.

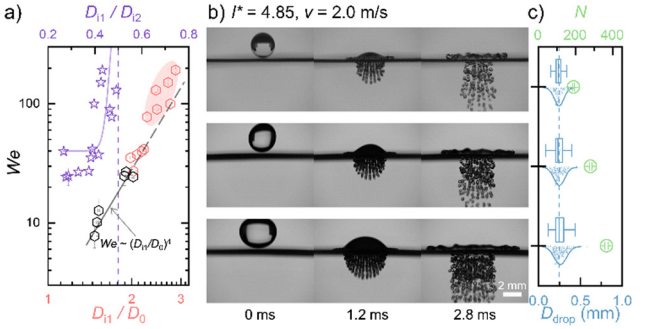


Fig. 3 Raindrops of different sizes can be transformed into microdroplets with a uniform diameter. (a) Plots of *We* number *versus* $D_{i1}/D_0$ and $D_{i2}/D_{i2}$, shown in the bottom axis and the top axis, respectively, where *I** = 4.85 (#100 superhydrophobic mesh). Black and red hexagonal dots represent unfragmented and fragmented drops, respectively. Without fragmentation, $We \sim (D_{i1}/D_0)^4$ is represented as a solid black line that extends with a dashed line. The red-shaded regime shows the cases of droplet fragmentation occurring. Purple stars represent the penetration efficiency values of #100 mesh, and tend to 0.5. (b) Image sequences showing almost identical fragmentations for different droplet diameters, for an impact velocity of 2.0 m $s^{-1}$. (c) Blue box chart illustrating the microdroplet diameter range for different raindrops after fragmenting. The microdroplet diameters were found to show small deviations and to be about 250 μm. Green dots represent the number of microdroplets (*N*) after fragmentation. Data in a and c are shown as mean ± SD, and each error bar represents SD ($n$ = 3, independent experiments). For each box plot in (c), the bounds and center line indicate the 25/75 percentiles and median values, and the upper and lower whiskers show maximum and minimum values.

and with the penetration factor thus decreasing gradually. To visualize the competition between spreading and penetration more directly, we put forward penetration efficiency, $D_{i2}/D_{i1}$, to represent the ability of a droplet to penetrate a pore to form a ligament. Our analyses indicated $D_{i2}/D_{i1}$ also being linearly proportional to *I**, and having an inflection point at $I$ = 4.85 (#100 mesh). Note the critical point being the smaller mesh size leading to a merging of adjacent ligaments. Our analyses indicated, for $I^* < 4.85$, the droplets becoming smaller with decreasing ligament width—and, for $I^* > 4.85$, ligaments merging before further disintegrating into microdroplets, leading to a reduction in penetration.

Taking into account that deformation, breaking-up and aggregation of raindrops occur during rainfall,[2,28] the impact-fragmentation of droplets of various sizes and moving at various velocities was also investigated. Droplets for which penetration had not occurred were shown to still follow the planar impact law $D_{i1}/D_0 \sim We^{1/4}$. But for droplets penetrating the mesh, the maximum spreading factor began to gradually deviate from this law (Fig. 3a). In addition, the penetration efficiency was found to gradually approach a constant value of 0.5 with increasing *We* number. This result suggested that the maximum penetration efficiency is only related to the superhydrophobic mesh. In other words, droplet fragmentation can occur as long as the inertial force meets the energy barrier required for penetration. We also statistically measured the size distribution ($D_{drop}$) and number of microdroplets (*N*) after fragmentation of different droplet sizes (Fig. 3b). At the same impact velocity, the number of fragmented microdroplets gradually increased as the droplet volume increased. However, microdroplet' size was uniform, with the distribution of their diameters showing them concentrated around 250 μm (Fig. 3c). This result suggested that the diameter of a fragmented microdroplet would also be determined by the size of the mesh for a droplet that can penetrate the mesh.

Finally, in order to investigate the feasibility of using this method for agricultural spraying, we set up a simple device and observed the growth of crops outdoor. The terminal speed of middle-sized raindrops approximately ranges from 20 cm $s^{-1}$ to 6 m $s^{-1}$,[12] and *We* number from 33 to 1400 constitute a typical range for raindrop impacts.[29] Compared to using other mesh numbers, using #100 superhydrophobic mesh was found to not only ensure fragmentation of most raindrops upon impact, but to also yield more uniform microdroplets. Fig. 4a shows an illustration of raindrops fragmenting into uniform microdroplets after impacting #100 superhydrophobic mesh. The fragmented microdroplets can be efficiently sprayed onto the crop leaves. To verify this concept, we prepared a 1.2 m × 1.2 m superhydrophobic mesh ($I$ = 4.85) by spraying it and fixing it on a simple frame with clips. A planting box for growing wheat in this simple device was placed at a distance of 550 mm from the mesh (Fig. 4b). Wheat seeds were evenly spread in 5 rows of 100 seeds in the planting box, and covered by a soil layer with a thickness $\Delta H$ of 30 mm (Fig. S3a, ESI†). During outdoor planting, the wheat growth process was recorded by using time-lapse cameras, and is shown in Mov. S1 (ESI†). Key frames

 

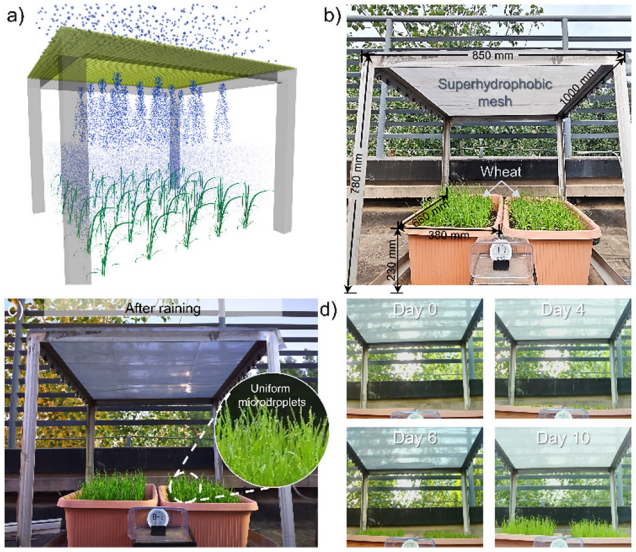


Fig. 4 Uniform spraying under a simple device with a #100 superhydrophobic mesh facilitates growth of wheat seedlings. (a) Schematic diagram of the concept of applying superhydrophobic meshes as roofs for smart spraying. (b) Dimensions of the simple device used for wheat cultivation. (c) After impacting the superhydrophobic mesh, the raindrops formed microdroplets that were uniformly sprayed on the wheat leaves. (d) Sequence of images of wheat seedling growth, specifically at days 0, 4, 6 and 10. A time-lapse recording of wheat growth is shown in Movie 1 (ESI†).

of uniform fragmented microdroplets covering the wheat leaves after rainfall are shown in (Fig. 4c). Also, chronophotography images of microdroplets resulting from fragmentation of raindrops on rainy days and irrigated waterdrops on sunny days are shown in Fig. S3b (ESI†). Inspection of these images indicated that large volumes of liquids can also be transformed into uniform microdroplets by impacting the mesh. A sequence of images of wheat seedling growth, at days 0, 4, 6 and 10, are shown in (Fig. 4d).

With the benefit of impact fragmentation, raindrops are able to spontaneously spray uniform microdroplets onto crops and achieve effective deposition. This method also provides a practical strategy for spraying pesticides manually in a lower dosage and more efficient way. Moreover, under the shield of the superhydrophobic mesh, the crop leaves would also be protected from the impact of heavy rainfall as well as from the direct rays of sunlight. Crop lodging and soil sloughing may be avoidable.

Overall, we have proposed the concept of a 'smart roof' fabricated using superhydrophobic meshes, and utilizing impact-fragmentation for agricultural spraying. Uniformly fragmented droplets can be transformed from raindrops or irrigated waterdrops impacting the mesh, and can even be pesticides or leaf fertilizers. A rapid spraying method that allows the fabrication of large-scale superhydrophobic metallic meshes has also been proposed, to meet the demands of large-scale applications.

Conceptualization: X. Deng, Z. Dong; methodology: T. Shen, C. Gao, and Z. Dong; investigation: T. Shen, C. Gao, S. Liu, Z. Liu, J. Peng, and J. Ma; visualization: T. Shen, and S. Liu; writing – original draft: T. Shen; writing – review & editing: Z. Dong and L. Jiang; supervision: X. Deng, Z. Dong, L. Bai and L. Jiang; funding acquisition: X. Deng, Z. Dong.

This work was financially supported by the National Natural Science Foundation of China (22122508), Natural Science Foundation of Hunan Province (2024JJ1005) and Huxiang Youth Talent Project Science and Technology Innovation (2023RC3028).

## Data availability

The data supporting this article have been included as part of the ESI.†

## Conflicts of interest

There are no conflicts to declare.

## Notes and references

1 E. Villermaux, *Annu. Rev. Fluid Mech.*, 2007, **39**, 419–446.
2 E. Villermaux and B. Bossa, *Nat. Phys.*, 2009, **5**, 697–702.
3 E. Villermaux and B. Bossa, *J. Fluid Mech.*, 2011, **668**, 412–435.
4 Y. Wang and L. Bourouiba, *J. Fluid Mech.*, 2018, **848**, 946–967.
5 T. Wang, Y. Si, N. Li, Z. Dong and L. Jiang, *ACS Nano*, 2019, **13**, 13100–13108.
6 N. Li, L. Wu, C. Yu, H. Dai, T. Wang, Z. Dong and L. Jiang, *Adv. Mater.*, 2018, **30**, 1703838.
7 S. R. G. Avila and C. D. Ohl, *J. Fluid Mech.*, 2016, **805**, 551–576.
8 S. Kooij, A. Astefanei, G. L. Corthals and D. Bonn, *Sci. Rep.*, 2019, **9**, 6128.
9 S. Zhou, L. Jiang and Z. Dong, *Chem. Rev.*, 2023, **123**, 2276–2310.
10 C. D. Modak, A. Kumar, A. Tripathy and P. Sen, *Nat. Commun.*, 2020, **11**, 4327.
11 S. Sharma, R. Pinto, A. Saha, S. Chaudhuri and S. Basu, *Sci. Adv.*, 2021, **7**, eabf0452.
12 D. Soto, H. L. Girard, A. Le Helloco, T. Binder, D. Quéré and K. K. Varanasi, *Phys. Rev. Fluids*, 2018, **3**, 083602.
13 J. Tang, X. Tong, Y. Chen, Y. Wu, Z. Zheng, A. B. Kayitmazer, A. Ahmad, N. Ramzan, J. Yang, Q. Huang and Y. Xu, *Nat. Commun.*, 2023, **14**, 6401.
14 R. Zhao, Q. Zhang, H. Tjugito and X. Cheng, *Proc. Natl. Acad. Sci. U. S. A.*, 2015, **112**, 342–347.
15 S. Liu, C. Zhang, T. Shen, Z. Zhan, J. Peng, C. Yu, L. Jiang and Z. Dong, *Nat. Commun.*, 2023, **14**, 5934.
16 B. Wang, J. Wang, C. Yu, S. Luo, J. Peng, N. Li, T. Wang, L. Jiang, Z. Dong and Y. Wang, *Global Challenges*, 2023, **7**, 2300007.
17 D. Soto, A. B. De Lariviere, X. Boutillon, C. Clanet and D. Quere, *Soft Matter*, 2014, **10**, 4929–4934.
18 I. Makhnenko, E. R. Alonzi, S. A. Fredericks, C. M. Colby and C. S. Dutcher, *J. Aerosol Sci.*, 2021, **157**, 105805.
19 S. Ryu, P. Sen, Y. Nam and C. Lee, *Phys. Rev. Lett.*, 2017, **118**, 014501.
20 C. Josserand and S. T. Thoroddsen, *Annu. Rev. Fluid Mech.*, 2016, **48**, 365–391.
21 Y. Fan, Y. Tan, Y. Dou, S. Huang and X. Tian, *Chem. Eng. J.*, 2023, **476**, 146485.
22 Z. Hu, F. Chu, H. Shan, X. Wu, Z. Dong and R. Wang, *Adv. Mater.*, 2024, **36**, 2310177.
23 G. Zhang, M. A. Quetzeri-Santiago, C. A. Stone, L. Botto and J. R. Castrejon-Pita, *Soft Matter*, 2018, **14**, 8182–8190.
24 S. A. Kooij, A. M. Moqaddam, T. C. de Goede, D. Derome, J. Carmeliet, N. Shahidzadeh and D. Bonn, *J. Fluid Mech.*, 2019, **871**, 489–509.
25 A. Kumar, A. Tripathy, C. D. Modak and P. Sen, *J. Microelectromech. Syst.*, 2018, **27**, 866–873.
26 Y. Y. Tang, M. J. Su, G. W. Chu, Y. Luo, Y. Y. Wang, L. L. Zhang and J. F. Chen, *Chem. Eng. Sci.*, 2019, **198**, 144–154.
27 K. Vontas, C. Boscariol, M. Andredaki, A. Georgoulas, C. Crua, J. H. Walther and M. Marengo, *Fluids*, 2020, **5**, 81.
28 A. P. Barros, O. P. Prat and F. Y. Testik, *Nat. Phys.*, 2010, **6**, 232.
29 Z. Wu, S. Basu, S. Kim, M. Sorrells, F. J. Beron-Vera and S. Jung, *Sci. Adv.*, 2024, **10**, eadj8092.